

# Effective study of operating parameters on the membrane distillation processes using various materials for seawater desalination

Abdelfatah Marni Sandid\*, Driss Nehari<sup>a</sup> and Taieb Nehari<sup>b</sup>

Department of Mechanical Engineering, University of Ain Temouchent, 46000 Ain Temouchent, Algeria

(Received November 23, 2021, Revised September 7, 2022, Accepted September 13, 2022)

**Abstract.** The paper presents the effect of operating temperatures and flow rates on the distillate flux that can be obtained from a hydrophobic membrane having the characteristics: pore size of 0.15  $\mu\text{m}$ ; thickness of 130  $\mu\text{m}$ ; and 85% porosity. That membrane in the present investigation could be the direct contact (DCMD) or the air-gap membrane distillation (AGMD). To model numerically the membrane distillation processes, the two-dimensional computational fluid dynamic (CFD) is used for the DCMD and AGMD cases here. In this work, DCMD and AGMD models have been validated with the experimental data using different flows (Parallel and Counter-current flows) in non-steady-state situations. A good agreement is obtained between the present results and those of the experimental data in the literature. The new approach in the present numerical modeling has allowed examining effects of the nature of materials (Polyvinylidene fluoride (PVDF) polymers, copolymers, and blends) used on thermal properties. Moreover, the effect of the area surface of the membrane (0.021 to 3.15  $\text{m}^2$ ) is investigated to explore both the laminar and the turbulent flow regimes. The obtained results found that copolymer P(VDF-TrFE) (80/20) is more effective than the other materials of membrane distillation (MD). The mass flux and thermal efficiency reach 193.5 ( $\text{g}/\text{m}^2\text{s}$ ), and 83.29 % using turbulent flow and an effective area of 3.1  $\text{m}^2$ , respectively. The increase of feed inlet temperatures and its flow rate, with the reduction of cold temperatures and its flow rate are very effective for increasing distillate water flow in MD applications.

**Keywords:** CFD; co-polymers; Membrane Distillation (MD); temperature polarization; thermal conductivity

## 1. Introduction

Desalination using membrane distillation (MD) can be described as the water treatment procedure applied by the temperature gradient over the micro-porous, hydrophobic membrane between the hot feed and the cold stream (permeate) (Anton and Olga 2018). Recently, the use of membrane distillation MD has been applied as a practical alternative solution to the use of conventional distillation and reverse osmosis (RO). The process occurs through the simultaneous transfer of mass and heat across the membrane: the water is evaporated on the hot side, while the water vapor is transported through the membrane. On the cold side, the water vapor is condensed (Ahmed *et al.* 2020).

Concerning the advantages of MD desalination, we can mention a low operating temperature (less than 100°C), high level of salt rejection with low fouling, and low operating pressure (Kalla 2021). Recent studies indicated that the materials used in the manufacture of MD technology are mainly polyvinylidene fluoride (PVDF), polytetrafluoroethylene (PTFE), or polypropylene (PP). The MD industry has been greatly developed within the last five decades (Li *et al.* 2019).

It is worth noting that the various commercial configuration of MD such as Direct Contact Membrane Distillation (DCMD), Air Gap Membrane distillation (AGMD), vacuum distillation (VMD), and gas scavenging distillation (SGMD) are used in industrial scale (Zhou *et al.* 2020). DCMD is one of the most widely used techniques due to the simplicity of operation as its thermal efficiency is related to energy use (thermal efficiency of the membrane). In MD application, AGMD technology's membrane thermal efficiency is higher than DCMD (Marni *et al.* 2021a). The AGMD technology has higher thermal energy efficiency because of the overlapping of the air gap that exists between the condensation zone and the membrane (Marni *et al.* 2021b).

Due to the air gap between condensation surfaces and the membrane, the AGMD configuration has the lowest heat transfer required when compared to other MDs. It also has better internal heat recovery, hence lower energy requirement, which makes it the first choice for a pilot plant for the work of Marni *et al.* (2021c). Although the effects of operating conditions have been reasonably studied, it is important to define parameter interactions and optimize the MD system to increase process performance and reduce energy consumption.

The MD configuration has been examined in the majority of CFD-based DCMD investigations. One reason for this could be the technology's simplicity when compared to other MDs, particularly for desalination and water/wastewater treatment (Parisa *et al.* 2019). On the other hand, Im *et al.* (2018) looked into CFD simulations of

\*Corresponding author, Ph.D. Student,  
E-mail: abdefatahsandid@hotmail.com

<sup>a</sup>Professor

<sup>b</sup>Ph.D.

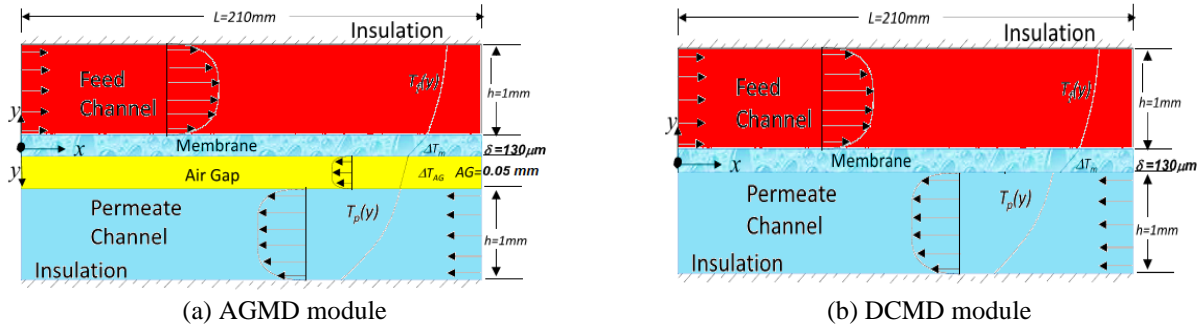


Fig. 1 Schematic diagram of the AGMD and DCMD modules

AGMD-based desalination to anticipate both heat and mass transport characteristics utilizing the composite membrane. On the hot side, they investigated the profiles of mass flux and temperature polarization next to the tubular membrane surface under various Reynolds numbers. The obtained results found that the temperature polarization can be decreased the distillate flux. It can be optimized by increasing the feed stream turbulence.

However, it should be noted that CFD simulation for the feed side in AGMD can produce the same results as DCMD technology. Besides, more efforts should be made to simulate the distillate side in AGMD, particularly the condensing surface (Mokhless *et al.* 2018). Furthermore, because the mass and heat transfer of AGMD technology may be more complicated than other technologies due to the mass/heat transfer resistance enforced by the air gap, more attempts at CFD simulation for this technology must be investigated.

The present paper investigates the mass and heat transfer in the liquid boundary layer of the PVDF membrane AGMD and DCMD applications using the commercial CFD code ANSYS-FLUENT with a new approach for this study. The present numerical modeling has allowed us to examine the effect of the nature of materials (Polyvinylidene fluoride (PVDF) polymers, copolymers, and blends) used on the thermal properties. Then, the effects of feed and cold inlet temperatures with flow rates on distillate flux average have been studied for seawater desalination. In addition, the mass flux, thermal efficiency, and temperature polarization coefficient (TPC) have been calculated using different areas and flow regimes (laminar and turbulent) of the AGMD process. Besides, effects of membrane physical properties and operating parameters (Temperatures and velocities), which occur on the membrane surface have an important significance for developing new membranes in the future.

## 2. AGMD and DCMD modules

A numerical study is performed on AGMD and DCMD by using ANSYS-FLUENT (CFD). Dimensions of 1 mm height and 210 mm length per channel with the thickness of 130  $\mu\text{m}$  for the DCMD module simulation, and adding to these an air gap of 0.05 mm for the AGMD module. A schematic diagram of the counter-current flows modules is illustrated in Fig. 1. The solution is calculated using the commercial CFD (code FLUENT) that's based on a

Table 1 Summary of PVDF, vapor, and total membrane thermo-physical properties

Material	Density (kg/m <sup>3</sup> )	Specific heat (J/kg K)	Conductivity (W/m K)	Viscosity (Pa)
PVDF	1775	1325	0.2622	-
Vapor	0.554	2014	0.0261	-
Membrane	302.2	1896.9	0.0662	-
Saline sea water (Doornbusch <i>et al.</i> 2020)	1013.2	4046.8	0.642	$5.86 \cdot 10^{-4}$
Pure water (Alotaibi <i>et al.</i> 2017)	995.2	4182.1	0.613	$8.38 \cdot 10^{-4}$

Table 2 Summary of boundary conditions for DCMD and AGMD

Boundary conditions	Feed channel	Permeate channel	Air-gap channel
Inlet channel	Kinetic	0.1 to 1 m/s	0.1 to 1 m/s
	Thermal	50 to 90°C	5 to 35°C
Outlet channel	Zero pressure, $dV/dx = 0$	Zero pressure, $dV/dx = 0$	Zero pressure, $dV/dx = 0$
Upper wall	Kinetic	Stationary/no-slip	Stationary/no-slip
	Thermal	Zero heat flux (insulated)	Coupled
Lower wall	Kinetic	Stationary/no-slip	Stationary/no-slip
	Thermal	Coupled	Zero heat flux

segregated solver and finite volume approach. The semi-implicit method for pressure equations (SIMPLE algorithm) is used for second-order upwind spatial derivatives and pressure-velocity coupling. Convergence residuals are set very tight at  $10^{-12}$  for all scalar equations, (energy, continuity, x- and y-momentums). All membrane, fresh feed, and saline permeate properties are listed in Table 1 (Janajreh *et al.* 2016), whereas a summary of the boundary conditions is shown in Table 2 (Janajreh *et al.* 2017).

## 3. Equation and methodology

### 3.1 Governing equations

The governing equations for the system are the conjugated steady incompressible Navier-Stokes and energy

equations are written as (Yang *et al.* 2019):

Continuity:

$$\frac{\partial u}{\partial x} + \frac{\partial v}{\partial y} = 0 \quad (1)$$

X-Momentum:

$$\frac{\partial u}{\partial t} + u \frac{\partial u}{\partial x} + v \frac{\partial u}{\partial y} = -\frac{1}{\rho} \frac{\partial p}{\partial x} + \nu \left( \frac{\partial^2 u}{\partial x^2} + \frac{\partial^2 u}{\partial y^2} \right) \quad (2)$$

Y-Momentum:

$$\frac{\partial v}{\partial t} + u \frac{\partial v}{\partial x} + v \frac{\partial v}{\partial y} = -\frac{1}{\rho} \frac{\partial p}{\partial y} + \nu \left( \frac{\partial^2 v}{\partial x^2} + \frac{\partial^2 v}{\partial y^2} \right) + \rho g_y \quad (3)$$

Energy:

$$\rho C_p \left( \frac{\partial T}{\partial t} + u \frac{\partial T}{\partial x} + v \frac{\partial T}{\partial y} \right) = k \left( \frac{\partial^2 T}{\partial x^2} + \frac{\partial^2 T}{\partial y^2} \right) + S_h \quad (4)$$

where  $u$  and  $v$  are the velocity components,  $\rho$  is the density,  $\mu$  is the viscosity,  $g_y$  is the gravitational acceleration,  $C_p$  is the specific heat,  $k$  is the thermal conductivity, and  $S_h$  is a source term of energy transport which is defined as follows:

$$\begin{cases} S_h = \frac{Q_{La}}{\delta_y} \times \frac{y_{mo}}{y_{mi}}; & \text{if } y = y_{mi} \\ S_h = -\frac{Q_{La}}{\delta_y} & ; \text{if } y = y_{mo} \\ 0 & ; \text{otherwise} \end{cases} \quad (5)$$

where  $Q_{La}$  is transmembrane latent heat flux at the hot side membrane surface, and  $y_{mo}$  and  $y_{mi}$  are the distance at  $y$ -direction of the inner and outer layer of membrane.  $\delta_y$  signifies the grid quantity in the  $y$ -direction.

### 3.2 Mass flux

The saturated pressure differential along membrane surfaces occurs because of temperature polarization while it drives mass transfer through the porous membrane.

The general mass flux expression is as follows (Cecília *et al.* 2019):

$$J = c_m (P_f^{sat} - P_p^{sat}) \quad (6)$$

where  $c_m$  is the membrane mass coefficient,  $P_f^{sat}$  and  $P_p^{sat}$  are the saturated water vapor pressures at the feed and permeate membrane surface, respectively.

The vapor pressure of distilled water and its temperature is described by the Antoine equation (Jincheng *et al.* 2019) within the range of the MD operation following a monotonic form and is written as:

$$P_{i(pure)}^{sat} = \exp \left( 23.238 - \frac{3841}{T - 45} \right), \quad i \{f, p\} \quad (7)$$

Three essential membrane coefficient models in the literature are stated to characterize the mass transfer across the microporous hydrophobic membrane (Attia *et al.* 2017): the Knudson, the Poiseuille flow, and the molecular diffusion models. However, in this paper, a combination of Poiseuille and Knudson models is described by:

$$c_m = c_k + c_p = 1.064 \alpha(T) \frac{\varepsilon r_p}{\tau \delta_m} \sqrt{\frac{M_w}{R T_m}} + 0.125 \beta(T) \frac{\varepsilon r^2}{\tau \delta_m} \frac{M_w P_m}{R T_m \mu_v} \quad (8)$$

where  $\alpha(T)$ , and  $\beta(T)$  are Knudsen diffusion and Poiseuille flow models contributions, respectively.  $T_m$  is mean membrane temperature ( $^{\circ}\text{C}$ ),  $M_w$  is the molar mass of the water in  $\text{kg/mol}$ ,  $P_m$  is mean pressure,  $R$  is gas constant,  $\delta_m$  thickness of the membrane,  $\mu_v$  is gas viscosity,  $\tau$  is tortuosity factor,  $r_p$  is pores radius, and  $\varepsilon$  is the membrane porosity.

### 3.3 Heat flux

The heat transfer in MD is characterized by three thermal resistances: Combined transfer over the membrane, convective and conductive transfers through the feed, and permeate boundary layers (ElKadi *et al.* 2020). The total heat flux in MD ( $Q_m$ ) is assigned to the latent heat of the evaporation ( $Q_v$ ) and a combination of the conduction ( $Q_c$ ). It is expressed as:

$$Q_m = Q_v + Q_c \quad (9)$$

Whereas the bulk membrane material is responsible for conduction, the membrane pores are responsible for evaporation. Taking  $\Delta H_m$  to be the enthalpy change because of the latent heat of the transmembrane mass flux, it is described by (Hesam *et al.* 2021):

$$Q_v = J \Delta H = J (H_{m,f} - H_{m,p}) \quad (10)$$

The conductive heat flux fraction is written by the Fourier heat equation as:

$$Q_c = -\frac{k_m}{\delta_m} (T_{m,f} - T_{m,p}) \quad (11)$$

where  $k_m$  is the equivalent thermal conductivity of the membrane.  $k_b$  and  $k_g$  are the bulk conductivity and the vapor conductivity of the weighted volume average. The subscripts  $f$  and  $p$  signify the feed and permeate, respectively.

### 3.4 Thermal efficiency and temperature polarization coefficient

The latent heat of evaporation used the total heat flux and the thermal efficiency is represented as:

$$\eta = \frac{Q_v}{Q_m} = \frac{J \Delta H_m}{Q_m} \quad (12)$$

Where the ratio of membrane boundary layer resistance over the total and bulk heat transfer resistance is defined by TPC or  $\theta$  as (Wu *et al.* 2017):

$$\theta = \frac{T_{m,f} - T_{m,p}}{T_{b,f} - T_{b,p}} = \frac{\Delta T_m}{\Delta T_b} \quad (13)$$

where the subscripts  $m$ ,  $p$ ,  $f$ , and  $b$  indicate the membrane permeate, feed and bulk surfaces, respectively. A small,

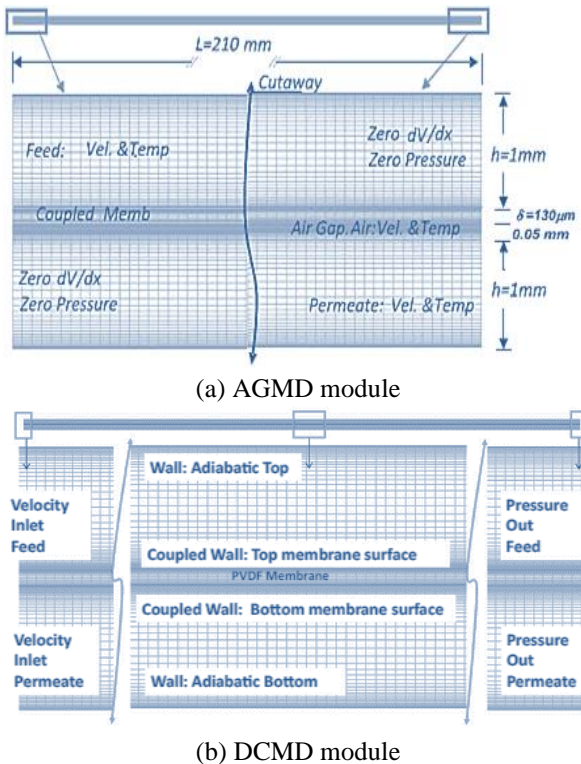


Fig. 2 The models' discretization mesh of AGMD and DCM

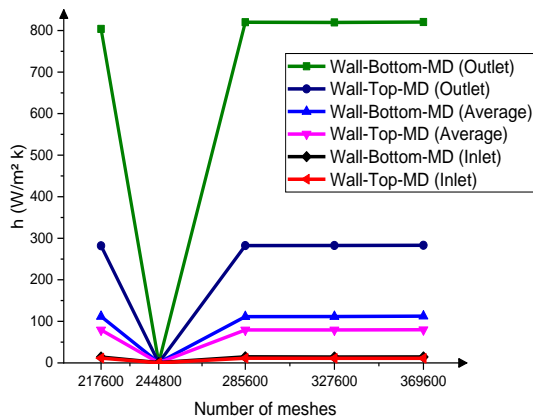


Fig. 3 Heat transfer coefficients ( $h$ ) at various mesh sizes

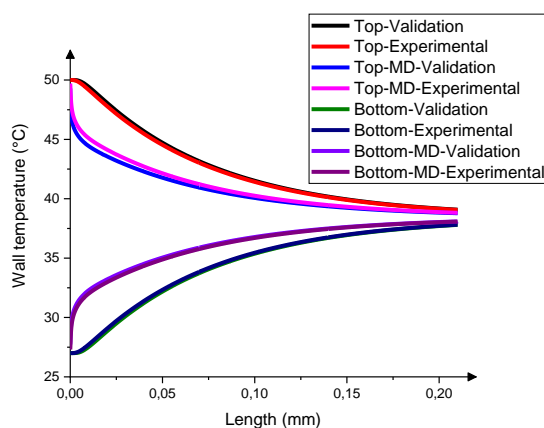


Fig. 4 Comparison between the experimental and simulation results of parallel flow surface temperatures in the DCM module

value of  $\theta$  ( $\leq 0.2$ ) signifies a limited heat transfer MD system.

#### 4. Grid Independent

Because the temperature and velocity profiles along the membrane's walls are so important, the grids are closely refined at those sides using the inflating layer. A grid independence study is carried out by putting various distributions to the test. For this study, the heat transfer coefficient ( $h$ ) is calculated using several grids and the trends of the change are shown in Fig. 2:

As shown in Fig. 2, meshing with 285600 grids presented the optimal results. Therefore, they are considered the chosen mesh in all cases using reasonable resolutions and a structured-quadrilateral type. The symmetrical two-dimensional flow systems are described in Fig. 3.

#### 5. Results and discussion

##### 5.1 Models validation

The present paper studies the mass and heat transfer in the liquid boundary layer of the PVDF membrane AGMD and DCM applications using the commercial CFD code ANSYS-FLUENT. The simulation results are validated with experimental data from Janajreh *et al* (2016). The system runs under the following operating conditions: hydrophobic PVDF membrane with a pore size of  $0.15 \mu\text{m}$ ; the thickness of  $130 \mu\text{m}$ ; Effective membrane area:  $0.021 \text{m}^2$  and 85% porosity running at Reynolds number of 10 ( $Re=V.h/\nu$ ), which is equivalent to  $0.01 \text{m/s}$  with an air gap  $0.05 \text{mm}$  for AGMD. In addition, the warmer feed temperature is  $50^\circ\text{C}$  and the cold permeate temperature is  $27^\circ\text{C}$ . As shown in Figs. 4 and 5, it can be noticed that the temperatures of the membrane and bulk surfaces at different flows (Parallel and Counter-current flow) calculated by the present model have good compatibility of no more than 5% in this experiment. In the membrane surfaces temperatures, the results show that the outlet cold temperatures increase to  $38^\circ\text{C}$  and  $43^\circ\text{C}$  in the parallel and counter-current flow respectively when the outlet hot temperatures decrease to  $39^\circ\text{C}$  and  $34^\circ\text{C}$ . Therefore, the outlet hot temperatures are more important in the case of "Counter-current flow" than in the "Parallel flow" case. Thus, the countercurrent configuration is retained and will be used in the remainder of this present paper.

In the AGMD module, the air gap is  $0.05 \text{mm}$  with keeping all other parameters and operating conditions constant as above. Fig. 6 shows a comparison between the results of this simulation and the applied results from Janajreh *et al.* (2017) that it made validation on the experimental research by Janajreh *et al.* (2016). The results show excellent compatibility between them. The results show that the outlet cold temperatures increase to  $44^\circ\text{C}$  and  $37^\circ\text{C}$  on the membrane and bulk surface temperatures respectively when the outlet hot temperatures decrease to  $36^\circ\text{C}$  and  $39^\circ\text{C}$ . It can be noticed that the membrane and bulk surface temperatures of the AGMD module predicted

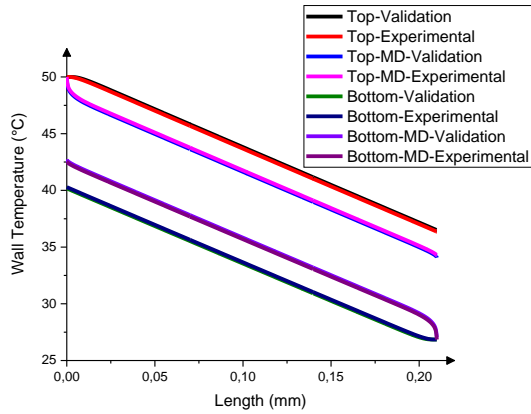


Fig. 5 Comparison between the experimental and simulation results of counter-current flow surface temperatures in the DCMD module

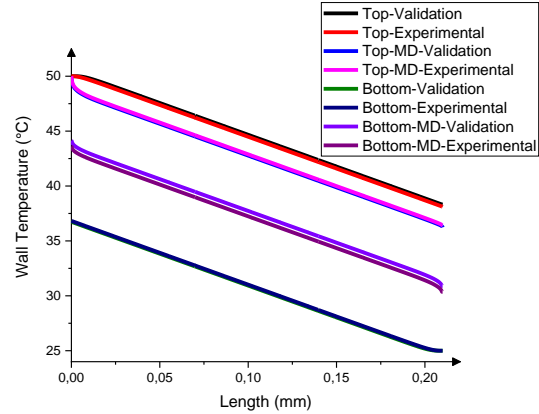


Fig. 6 Comparison between the experimental and simulation results of membrane and bulk surface temperatures in the AGMD module

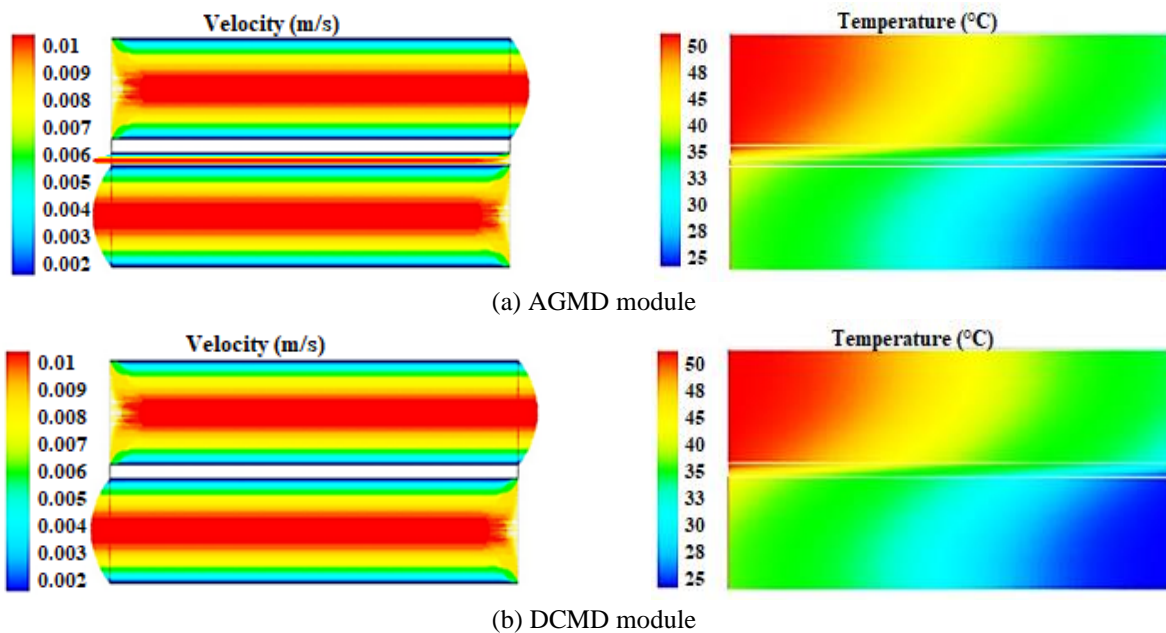


Fig. 7 Velocity vectors and Temperature contours: (a) AGMD and (b) DCMD modules

by the present model have a good agreement as shown in Fig. 6.

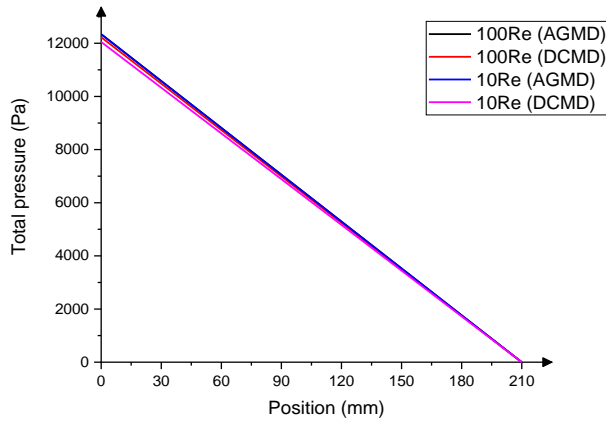
5.2 Temperature contours, velocity vectors, and total pressures of the AGMD and DCMD modules

The thermal behavior of the fluid in AGMD and DCMD modules is shown in Fig. 7(a). First, note that the velocity vectors coming from the inlet and heading towards the outlet on both sides of the fluid confirm the direction of flow and subsequently the counter-current configuration in both AGMD and DCMD modules. As shown in Fig. 7(b), it is seen that the heat exchange happens between the hot fluid and the internal wall by convection, then by conduction through the thickness of the membrane, and finally by convection between the outer wall of the membrane and the fluid. We also note that the exchange is more important the more presides over the wall and especially at the outlets of the AGMD and DCMD modules.

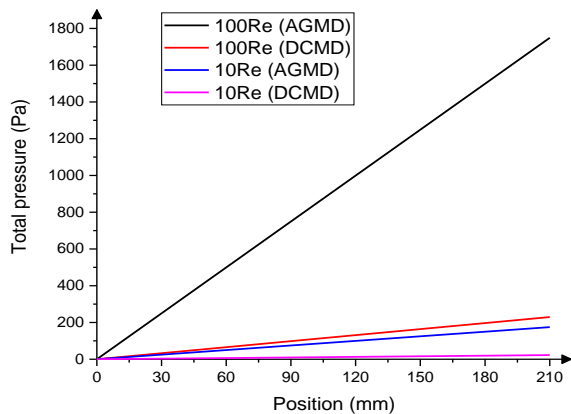
Fig. 8 shows the distribution of pressure along the membrane length feed and permeates sides of AGMD and DCMD. Between the AGMD and DCMD modules, the total pressures reach 12338 Pa and 12052 Pa at Re=10, while they reach 12345 Pa and 12229 Pa at Re=100 respectively on the feed side. However, they reach 174 Pa and 22 Pa at Re=10 while they reach 1748 Pa and 229 Pa at Re=100 respectively on the permeate side. Therefore, the membrane length feed side is more effective than the permeate side of MD. However, AGMD is better than DCMD since permeate is condensed on a cold surface in AGMD rather than in direct contact on the permeate side in DCMD. Furthermore, the air gap separates the membrane from a condensed surface, which is the primary advantage of AGMD against all other MD applications. In the DCMD operation, the surface tension is lower and the contact angle is smaller with the membrane.

Thus, the permeate side of the membrane is probably to be wet. In opposition, the concentration of the condensed





(a) AGMD module



(b) DCMD module

Fig. 8 Distribution of pressure along the membrane length in AGMD and DCMD

permeate in AGMD isn't in direct contact with the membrane surface, hence there isn't a risk of membrane wetness on the permeate side. Therefore, the AGMD configuration is retained and will be used in the remainder of this present paper.

### 5.3 Effect of operating temperatures

In order to study the influence of inlet feed temperature on mass flux, the feed temperature varies from 50°C to 90°C. The system is run under the following operating conditions: hydrophobic PVDF membrane with a pore size of 0.15  $\mu\text{m}$ , a thickness of 130  $\mu\text{m}$ , Effective membrane area: 0.021  $\text{m}^2$ , and 85% porosity running at a velocity of 10 with an air gap of 0.05 mm. Fig. 9 shows the result of the modeling study at selected inlet cold temperatures of 15, 25, and 35°C. It can be seen that increasing the feed temperature increases the system flux significantly. Increasing the feed temperature increases the vapor production and the driving force to permeation (the transmembrane temperature difference, and consequently the difference at partial pressures along membrane surfaces) which enhances permeation across the membrane. The percentage increase in flux when the feed temperature is increased from 50°C to 90°C is 89% at the cold temperature of 35°C, 85% at 25°C, and 83% at 15°C. Thus, percentage-wise, a higher cold temperature gives more percentage increase in mass flux.

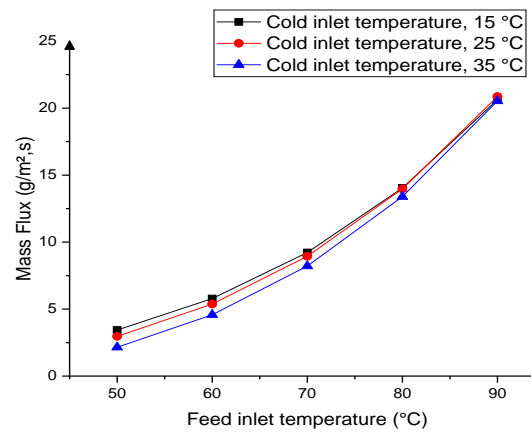


Fig. 9 Effect of feed inlet temperature on mass flux

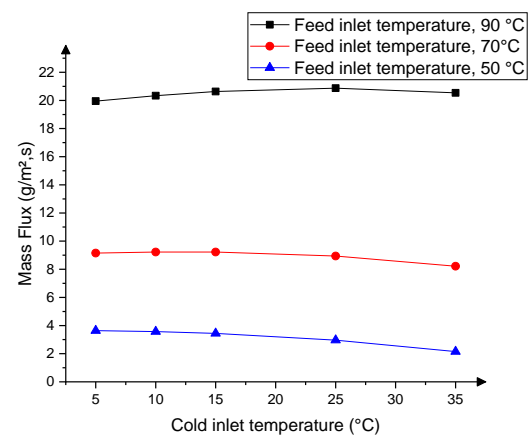


Fig. 10 Effect of cold inlet temperature on mass flux

The effect of cold inlet temperature observes at selected different feed inlet temperatures of 50, 70, and 90°C. The modeling study is performed under the same conditions as above (hydrophobic PVDF membrane with a pore size of 0.15  $\mu\text{m}$ , the thickness of 130  $\mu\text{m}$ , Effective membrane area: 0.021  $\text{m}^2$ , and 85% porosity running at a velocity of 0.1 with an air gap of 0.05 mm). It observes that for a given feed temperature, by decreasing the cold temperature, mass flux increases as shown in Fig. 10. Decreasing the cold temperature increases the difference of partial pressure that assists the permeation process across the membrane. Percentage-wise, reducing the cold temperature from 35°C to 5°C results in the mass flux increase of 2% at feed temperature of 90°C, 10% at feed temperature of 70°C, and 41% at feed temperature of 50°C.

### 5.4 Effect of operating flow rates

In order to investigate the effect of Reynolds number (Re) in the feed side on the mass flux; the modeling study is conducted with variable feed flow rates while keeping all other parameters constant. The feed flow rate varies from 0.01 m/s to 0.1 m/s (10Re to 100Re). The operating conditions for the simulation are; a hydrophobic PVDF membrane with a pore size of 0.15  $\mu\text{m}$ , a thickness of 130  $\mu\text{m}$ , an effective membrane area of 0.021  $\text{m}^2$ , 85% porosity, and an air gap of 0.05 mm with permeate temperature 25°C

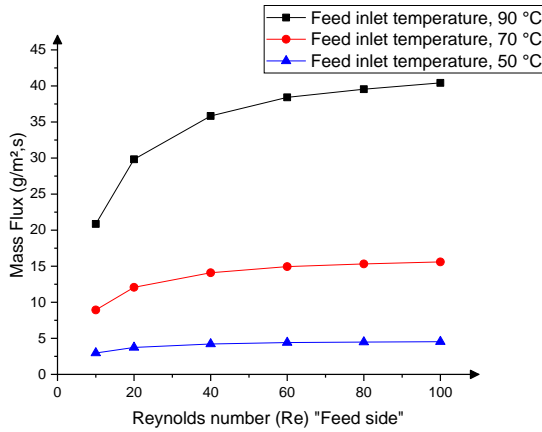


Fig. 11 Effect of Reynolds number (Feed side) on mass flux

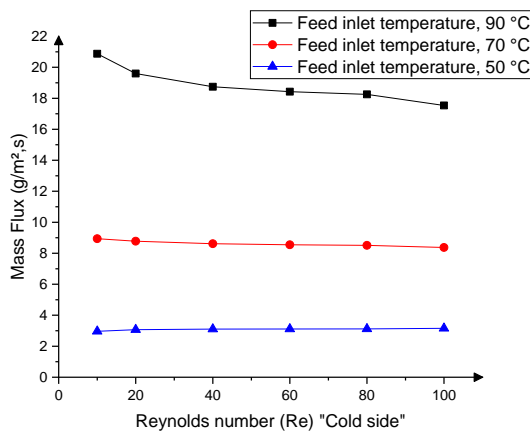


Fig. 12 Effect of Reynolds number (Cold side) on mass flux

and cold flow rate 0.1 m/s. Fig. 11 shows the variation of mass flux with feed flow rate for selected feed temperature of 50, 70 and 90°C. The trend shows that increasing the feed flow rate increases the mass flux substantially. Feed flow rate is a very effective variable to increase the system flux at different feed temperatures. It is worth mentioning that the exponential nature of flux increase can better be observed at 90°C as compared to other feed temperatures of 50 and 70°C. Over the entire range of feed flow rate, (0.01 to 0.1 m/s) 48% increase in mass flux is obtained at a feed temperature of 90°C, 43% is obtained at 70°C and 35% is obtained at 50°C.

In order to examine the effect of Re on the cold side; the cold flow rate varies from 0.01m/s to 0.1m/s (10Re to 100Re) while keeping all other parameters constant. The operating conditions for the modeling study are; a hydrophobic PVDF membrane with a pore size of 0.15 μm, a thickness of 130 μm, an effective membrane area of 0.021 m², 85% porosity, and an air gap of 0.05 mm with permeate temperature of 25°C and feed flow rate 0.01 m/s.

Fig. 12 shows the variation of mass flux with cold flow rate for selected feed temperatures of 50, 70, and 90°C. The trends show that increasing the cold flow rate increases the mass flux marginally. Cold flow rate seems more effective at high feed temperature as compared to low feed temperature.

Table 3 Thermal properties of different materials of MD (Iguchi *et al.* 2007)

No.	Materials of MD	Specific heat (J/kgK)	Density (kg/m³)	Thermal diffusivity (*10 <sup>-6</sup> m²/s)	Thermal conductivity (W/m K)
1	PVDF	1325	1775	0.1115	0.2622
2	PVDF/P(VDF-TrFE) (70/30)	1172	1938	0.0797	0.1810
3	PVDF/P(VDF-TrFE) (50/50)	1049	2067	0.1473	0.3193
4	P(VDF-TrFE) (80/20)	1092	1657	0.0934	0.1690
5	P(VDF-TrFE) (70/30)	1159	1786	0.943	0.1952
6	P(VDF-TrFE) (50/50)	1066	1936	0.1029	0.2123

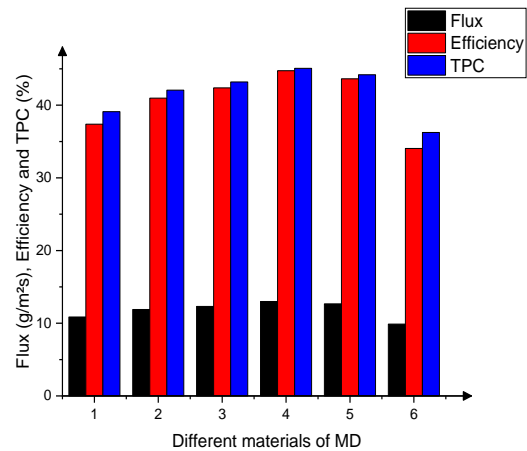


Fig. 13 Thermal efficiency, mass flux, and TPC on different materials of MD

Over the entire range of the tested cold flow rate (0.01 to 0.1 m/s), only a 15 % increase in flux is obtained at 90°C, 6.4 % increase in flux at 70°C, and 6.1% is obtained at 50°C.

### 5.5 Effects of different thermal properties on various materials of MD

All Thermal properties of different materials (Polyvinylidene fluoride (PVDF) polymers, copolymers, and blends) are shown above in Table 3.

Fig. 13 shows the thermal efficiency, mass flux, and TPC on different Materials of MD. The feed inlet temperature is 70°C while keeping all other parameters constant. The operating conditions for the simulation are; a hydrophobic PVDF membrane with a pore size of 0.15 μm, a thickness of 130 μm, an effective membrane area of 0.021 m², an air gap of 0.05 mm, and 85% porosity with a cold temperature of 25°C and feed flow rate 0.01 m/s. It can be seen that the copolymer P(VDF-TrFE) (80/20) is better than the other materials. In addition, the mass flux, thermal efficiency, and TPC reach 12.99 (g/m².s), 44.74%, and 45.06 respectively. As shown in Table 3 and Fig. 13, if the density and thermal conductivity are lower, the thermal efficiency, mass flux, and TPC of MD are higher and more effective for seawater desalination.

Table 4 Comparison of different membrane parameters using different flow regimes

Effective membrane area (m <sup>2</sup> )	0.021	1.05	2.1	2.1	3.15
Feed and permeate flow rates (m/s)	0.01	0.1	0.05	0.1	1
Flow regimes	Laminar	Laminar	Laminar	Turbulent	Turbulent
Flux average (g/m <sup>2</sup> s)	12.99	64.5	118.95	129	193.5
Thermal efficiency(%)	44.74	54.52	68.27	74.04	83.29
Effective membrane area (m <sup>2</sup> )	0.021	1.05	2.1	2.1	3.15

### 5.6 Effects of different areas and flow regimes

Table 4 shows the comparison of different membrane parameters (area and flow rates) using different flow regimes (laminar and turbulent). The used material of MD is the hydrophobic copolymer P(VDF-TrFE) (80/20) while keeping all other parameters constant ( the pore size of 0.15  $\mu\text{m}$ , the thickness of 130  $\mu\text{m}$  and 85% porosity with feed inlet temperature is 70°C and cold temperature 25°C).

The variations in the different membrane parameters are very effective to produce distillate water. As shown in Table 4, if the membrane area and flow rates increase the flux average of distillate water increases. Therefore, they have a significant effect on increasing the average flow rate. Moreover, the mass flux and thermal efficiency reach 118.95 (g/m<sup>2</sup>s), and 68.27 % with the laminar flow regime and they reach 193.5 (g/m<sup>2</sup>s), and 83.29% with the turbulent flow regime, respectively. Therefore, the model turbulent is better than the laminar flow regime. In addition, increasing the feed flow rate and the area of MD is increased the mass flux and thermal efficiency.

## 6. Conclusions

Symmetrical 2D flow systems are performed on AGMD and DCMD using non-isothermal CFD coupled thermally with the solid porous membrane. In the membrane surface temperatures, the outlet hot temperatures are more important in the case (Counter-current flow) than (Parallel flow). The thermal behavior of the fluid in AGMD and DCMD modules notes that the exchange is more important the more presides over the wall and especially at the outlets of the AGMD and DCMD modules. Between the AGMD and DCMD modules, the total pressures reach 20 Pa to 1750 Pa at 10Re and 100Re respectively. However, AGMD is better than DCMD since permeate is condensed on a cold surface in AGMD rather than in direct contact on the permeate side in DCMD. Moreover, the concentration of the condensed permeate in AGMD isn't in direct contact with the membrane surface, hence there isn't a risk of membrane wetness on the permeate side.

Increasing the feed temperature increases the vapor production and the driving force to permeation, which enhances permeation along the membrane surface. Decreasing the cold temperature increases the difference of

partial pressure that assists the permeation process across the membrane. The variation of mass flux with feed flow rate shows that increasing the feed flow rate increases the mass flux substantially. In addition, increasing the cold flow rate increases the flux marginally.

The copolymer P(VDF-TrFE) (80/20) is better than the other materials of MD. The flux average, thermal efficiency, and TPC reach 12.99 (g/m<sup>2</sup>s), 44.74 and 45.06 % respectively. The lower density and thermal conductivity are more effective for increasing the distillate water flow in AGMD processes. In addition, the mass flux and thermal efficiency reach 68.27 (g/m<sup>2</sup>s), and 68.27 % with the laminar flow regime and they reach 193.5 (g/m<sup>2</sup>s), and 83.29 % with the turbulent flow regime, respectively. Therefore, the variations in the different membrane parameters are very effective and the turbulent flow regime is better than the laminar flow regime. Finally, this effective study will be useful to develop and optimizing in the future both the small and large scales MD processes for desalination.

## Acknowledgments

The authors acknowledge the financial supports of the FNRSDT/DGRSDT within the framework of ERANETMED3 (Project.ERANETMED3-166EXTRASEA)

## References

- Ahmed, F.E., Lalia, B.S., Hashaikeh R. and Hilal N. (2020), "Alternative heating techniques in membrane distillation: A review", *J. Desal.*, **496**, 1-14. <https://doi.org/10.1016/j.desal.2020.114713>.
- Alotaibi, S., Ibrahim, O.M., Luo, S. and Luo, T. (2017), "Modeling of a continuous water desalination process using directional solvent extraction", *J. Desal.*, **420**, 114-124. <https://doi.org/10.1016/j.desal.2017.07.004>.
- Anton, A.K. and Olga, M.K.R. (2018), "An industrial perspective on membrane distillation processes", *J. Chem. Tech. Biotech.* **93**(8), 2047-2055. <https://doi.org/10.1002/jctb.5674>.
- Attia, H., Osman, M. S., Johnson, D.J., Wright, C. and Hilal, N. (2017), "Modelling of air gap membrane distillation and its application in heavy metals removal", *J. Desal.*, **42**, 427-436. <https://doi.org/10.1016/j.desal.2017.09.027>.
- Cecília, M.S.A., Luiza, B.G., Ramatisa, L.R., Cíntia, S.M., and Míriam, C.S.A. (2019), "Bi-dimensional modelling of the thermal boundary layer and mass flux prediction for direct contact membrane distillation", *Int. J. Heat Mass Transf.*, **141**, 1205-1215. <https://doi.org/10.1016/j.ijheatmasstransfer.2019.07.014>.
- Doornbusch, G.J., Bel, M., Tedesco, M., Post, J.W., Borneman, Z. and Nijmeijer, K. (2020), "Effect of membrane area and membrane properties in multistage electro dialysis on seawater desalination performance", *J. Membr. Sci.*, **611**, 118303. <https://doi.org/10.1016/j.memsci.2020.118303>.
- ElKadi, K., Janajreh, I. and Hashaikeh, R. (2020), "Numerical simulation and evaluation of spacer-filled direct contact membrane distillation module", *Appl. Water. Sci.*, **10**, 174. <https://doi.org/10.1007/s13201-020-01261-9>.
- Hesam, B.H., Asadi, A., Shen, Z.G., Rahnama, M., Djilali, N. and Sui, P. (2021), "Modeling of heat and mass transfer in direct contact membrane distillation: Effect of counter diffusion



- velocity”, *J. Desal. Water Treat.*, **216**, 71-82.  
<http://doi.org/10.5004/dwt.2021.26816>.
- Iguchi, C.Y., Santos, W.N. and Gregorio, R. (2007), “Determination of thermal properties of pyroelectric polymers, copolymers and blends by the laser flash technique”, *Polym. Test.*, **26** 788-792.  
<https://doi.org/10.1016/j.polymertesting.2007.04.009>.
- Im, B.G., Lee, J.G., Kim, Y.D. and Kim, W.S. (2018), “Theoretical modeling and simulation of AGMD and LGMD desalination processes using a composite membrane”, *J. Membr. Sci.*, **565**, 14-24.  
<http://doi.org/10.1016/j.memsci.2018.08.006>.
- Janajreh, I., Elkadi, K., Hashaikeh, R. and Ahmed, R. (2017), “Numerical investigation of air gap membrane distillation (AGMD): Seeking optimal performance”, *J. Desal.*, **424**, 122-130. <https://doi.org/10.1016/j.desal.2017.10.001>.
- Janajreh, I., Suwwan, D. and Hashaikeh, R. (2016), “Assessment of direct contact membrane distillation under different configurations, velocities, and membrane properties”, *Appl. Energy*, **185**, 2058-2073.  
<https://doi.org/10.1016/j.apenergy.2016.05.020>.
- Jincheng, L., Johan, V., Steven, C.D., Tzahi, Y.C. and Nils, T. (2019), “Computational fluid dynamics simulations of polarization phenomena in direct contact membrane distillation”, *J. Membr. Sci.*, **591**, 117150.  
<https://doi.org/10.1016/j.memsci.2019.05.074>.
- Kalla, S. (2021), “Use of membrane distillation for oily wastewater treatment—a review”, *J. Env. Chem. Eng.*, **9**(1), 1-59.  
<https://doi.org/10.1016/j.jece.2020.104641>.
- Li, Z., Rana, D., Matsuura, T., Teoh, C.Q.L. and Chung, T. (2019), “The performance of polyvinylidene fluoride-polytetrafluoroethylene nanocomposite distillation membranes: An experimental and numerical study”, *Sep. Purif. Tech.*, **226**, 192-208 <https://doi.org/10.1016/j.seppur.2019.05.102>.
- Marni-Sandid, A., Bassyouni, M., Nehari, D., Elhenawy, Y., (2021a) “Experimental and simulation study of multichannel air gap membrane distillation process with two types of solar collectors”, *Energy Convers. Manag.*, **24**, 31-14.  
<https://doi.org/10.1016/j.enconman.2021.114431>.
- Marni-Sandid, A., Nehari, D., Elmeriah A. and Remlaoui, A. (2021c), “Dynamic simulation of an air-gap membrane distillation (AGMD) process using photovoltaic panels system and flat plate collectors”, *J. Therm. Eng.*, **7**, 117-133.  
<https://doi.org/10.18186/thermal.870383>.
- Marni-Sandid, A., Nehari, T. and Nehari, D., (2021b) “Simulation study of an air-gap membrane distillation system for seawater desalination using solar energy”, *J. Desal., Water Treat.*, **229**, 40-51. <https://doi.org/10.5004/dwt.2021.27394>.
- Mokhless, B., Sofiene, K., Mohamedn B.B.H. and Habib, B.B. (2018), “Simulation and experimental study of an AGMD membrane distillation pilot for the desalination of seawater or brackish water with zero liquid discharged”, *Int. J. Heat Mass Transf.*, **54**, 3521-3531.  
<https://doi.org/10.1007/s00231-018-2383-6>.
- Parisa, B., Niloofar, T.A., Mohammad, A.M. and Mohammad, R.R., (2019), “Water and wastewater treatment systems by novelintegrated Membrane Distillation (MD)”, *J. Chem. Eng.*, **3**(8), 1-36. <http://doi.org/10.3390/chemengineering3010008>.
- Wu, J., Zodrow, K.R., Szemraj, P.B., Li, Q. (2017), “Photothermal nanocomposite membranes for direct solar membrane distillation”, *J. Mater. Chem. A.*, **5**, 23712-23719.  
<https://doi.org/10.1039/C7TA04555G>.
- Yang, L. M.,Shu, C., Yang, W. M. and Wu,J.(2019), “Simulation of conjugate heat transfer problems by lattice Boltzmann flux solver”, *Int. J. Heat Mass Transf.*, **137**, 895-907.  
<https://doi.org/10.1016/j.ijheatmasstransfer.2019.04.003>.
- Zhou, J., Wang, F., Noor, N. and Zhang, X. (2020), “An experimental study on liquid regeneration process of a liquid desiccant air conditioning system (LDACs) based on vacuum membrane distillation”, *J. Energy*, **194**, 1-9.  
<https://doi.org/10.1016/j.energy.2019.116891>.

ED